Image Processing for Planetary Limb/Terminator Extraction

SURAPHOL UDOMKESMALEE, DAVID Q. ZHU AND CHENG-CHIH CHU

Jet Propulsion Laboratory, California Institute of Technology
Pasadena, California 91109

Dr. Suraphol Udomkesmalee
Jet Propulsion Laboratory
4800 Oak Grove Drive
Pasadena, CA 91109-8099

Tel: (81 8) 354-0614
Fax: (81 8) 353-6478

ABSTRACT

A novel image segmentation technique for extracting limb and terminator of planetary bodies is proposed. Conventional edge-based histogramming approaches are employed to trace object boundaries. The limb and terminator bifurcation is achieved by locating the harmonized segment in the two equations representing the 2-D parametrized boundary curve. This technique is quite efficient and robust. Although only spherical (near-spherical) planetary bodies in full view are addressed in details, the proposed methodology can be extended to accommodate partially viewed and/or arbitrary-shaped objects; formulations for these cases are also given. Real planetary images from Voyager 1 and 2 serve as representative test cases to verify the proposed methodology.

LIST OF SYMBOLS

$x(t)$	*parametric x-function*	2nd paragraph, page 6; Eq. (1), page 11; 1st, 2nd, 3rd paragraph, page 1; 2nd paragraph, page 12; 1st paragraph, page 14; Eq. (4), Eq. (5), Eq. (6), 1st, 2nd, 3rd paragraph, page 15; Eq. (7), Eq. (9), page 21;
$y(t)$	*parametric y-function*	1st paragraph, page 6; Eq. (l), page 11; 1st paragraph, page 11; 2nd paragraph, page 12; 1st paragraph, page 14; Eq. (4), Eq. (5), Eq. (6), 1st, 3rd paragraph, page 15; Eq. (7),@. (8), Eq. (9), page 21;
R	*planet radius*	Eq. (1), page 11; 1st paragraph, page 11; Eq. (4), Page 15; Eq. (7), Eq.(8), page 21;
ϕ	*phase angle*	Eq. (l), page 11; 1st paragraph, page 11; Eq. (4), Eq. (5), Eq. (6), page 15; Eq. (7), Eq. (8), page 21;
μ_x	*mean x-position*	Eq. (1), page 11; Eq. (2), 1st, 2nd, 3rd, 4th paragraph, page 11; 2nd paragraph, page 12; Eq. (4), Eq. (5), Eq. (6), 1st, 2nd paragraph, page 15; Eq. (7), Eq. (8), 2nd paragraph, page 21;
μ_y	*mean y-position*	Eq. (l), page 11; 1st paragraph, page 11; Eq. (4), Eq. (5), page 15; Eq. (7), page 21;
t	*path length*	Eq. (1), page 11; 1st paragraph, page 11; 1st paragraph, page 14; Eq. (5), Eq. (6), page 15; Eq. (7), Eq. (8), page21;
$\mathbf{D}_t$	*differential operator*	1st paragraph, page 11; 2nd paragraph, page 12; 1st paragraph, page 15; Eq. (6), page 15; 1st paragraph, page 15; Eq. (8), page 21;
π	*pi*	Eq. (l), page 11; 1st paragraph, page 11; 1st paragraph, Eq. (4), Eq. (5), Eq. (6), page 15; 3rd paragraph, page 16; Eq. (7), Eq. (8), 1st, 2nd paragraph, page 21;
$\tilde{y}(t)$	*harmonized function*	Eq. (2), 2nd, 3rd paragraph, page 11; 2nd paragraph, page 12; 1st paragraph, page 14; Eq. (6), 2nd paragraph, page 15; 1st paragraph, Eq. (8), page 21;
A_k	*accumulator array*	3rd, 4th paragraph, page 11;
x_i	*indexed x-array*	Eq. (3), 3rd paragraph, page 11; 2nd paragraph, page 12;
$\tilde{y}_i$	*indexed y-array*	Eq. (3), 4th paragraph, page 11; 2nd paragraph, page 12;
μ_k	*indexed p-array*	Eq. (3), 3rd paragraph, page 11;
τ	*tolerance*	Eq. (3), 3rd paragraph, page 11;
$\hat{A}$	*maximum of* A_k	4th paragraph, page 11;
k_a	*left index*	4th paragraph, page 11;
k	*index variable*	4th paragraph, page 11;
k_b	*right index*	4th paragraph, page 11;
k^*	*midpoint index*	4th paragraph, page 11;
τ^*	*adjusted tolerance*	4th paragraph, page 11; 2nd paragraph, page 12;
μ_{k^*}	*estimated mean x-value*	4th paragraph, page 11;
Δt	*path length increment*	1st paragraph, page 14;
$\sqrt{2}$	*square root of two*	1st paragraph, page 14;
f	*frequency*	Eq. (4), 1st paragraph, page 15; Eq. (7), Eq. (8), 1st, 2nd paragraph, page 21;
R_x	*planet x-radius*	Eq. (5), Eq. (6), 2nd paragraph, page 15;
R_y	*planet y-radius*	Eq. (5), Eq. (6), 2nd paragraph, page 15;
t'	*unnormalized t*	Eq. (9), 1st paragraph, page 22.

1. INTRODUCTION

Image processing of planetary scenes is an essential element of onboard autonomous pointing and control of planetary exploration spacecraft [1]. Planetary limb (i.e., the illuminated edge of a planet or a planetary satellite) and terminator (i.e., the boundary between day and night of a planet or a planetary satellite) data can provide references for determining the desired target-spacecraft location, and planet shape and size. Any error resulting from such feature extraction can be detrimental to the mission, which may rely on the target-relative information to maneuver the spacecraft and autonomously capture important scientific data during a brief encounter period. The boundaries of celestial objects can be extracted using an edge-based histogramming method similar to the typical segmentation of a computer vision system to separate objects from the background [2]-[3] (note the dark background with few stars in our applications). Although many segmentation techniques have been proposed, the methodology to extract limb and terminator features of celestial objects has never been fully addressed, and current solutions based on some *a priori* topographic/photometric models [4] are not reliable because of terrain variations which are extremely difficult to automate. Hence, constrained by onboard computing power, robustness requirements, and the lack of *a priori* knowledge about the planetary terrains, we seek a germane limb/terminator extraction solution for planetary images.

Figure 1 depicts a typical scene demanding accurate characterization of planetary limb and terminator. Because the image contains a bright object and dark background, an "automatic thresholding technique placing the threshold in the valley between two modes of the histogram [5] provides a reasonable means of isolating the desired celestial object and its boundary points. Given the object boundary points, the determination of limb and terminator is not trivial. The terrains along the terminator can provide strong edge-segments that are comparable to those of limb segments, thus rendering a piecewise edge strength discrimination ineffective. By the same token, the true limb can have weak edge-segments because of shadowing and/or discoloration on terrains, and thus differentiating the limb from terminator will require a more elegant solution.

Limb/terminator extraction for the planetary body shown in Fig. 1 has become a major issue in planetary exploration with autonomous spacecraft. Knowing the set of limb points of a spherical body, one can accurately determine its position (center of mass) and relative size through circle fitting and plan a mosaic sequence to capture close-up high-resolution images [6]. Pointing operations for future missions like Pluto Fast Flyby [7] will probably require this type of image analysis to achieve autonomous target-relative pointing because the round-trip communication times and flyby speed prohibit ground-based spacecraft maneuvering and planning. Accurate segmentation of limb and terminator can also provide information pertaining to Sun-relative spacecraft position that can be used to navigate the spacecraft, an avenue which has never been explored,

Fig. 1. A planetary image of a Uranus moon (Miranda) taken by Voyager 2.

We have also considered and experimented with alternative solutions such as the Hough transform for circles [S] and curvature representation [9]-[10] for this limb/terminator bifurcation. However, the conventional Hough transformis found to be too computationally expensive because ofthe multi-dimensional parameter space, and gauging the proper ranges and resolutions ofthese unknown parameters can be difficult. In addition, because a circular arc can reasonably approximate the terminator of spherical objects, the use of Hough transform to determine the limb and terminator of celestial objects is not trivial. On the other hand, the curvature representation is found to be very noisy because of the required computation of first and second derivatives, and deciding the location of the two break points along the boundary that separate the limb from terminator based on contour curvature is also non-trivial.

In this paper, we derive an efficient and robust algorithm to extract the limb and terminator by parametrizing the boundary curve based on the path length *(t)* and rely on the harmonization of parametric functions [*x(t),* y(t)] defined on the limb to differentiate it from terminator. Note that the boundary we will be referring to throughout this paper is not the true planet boundary, but rather the illuminated area bounded by the darkness of the background or the unilluminated portion of the planet body. Considering that most planetary bodies are spherical, the limb is a circular arc (which implies sinusoidal parametric equations), and the terminator (although can be near-circular) is often erratic because of terrain variations" and planet geometry. By examining the two parametric functions, the limb portion represented in x(t) and *y(t)* will be homologous except for a 90 degree phase shift. The harmonization is achieved by a differential operator applied to *y(t)* and then compared with *x(t).* Experiments with real planetary images from Voyager 1 and 2 confirm the robustness of this approach. In addition, formulations to accommodate partially-viewed objects (i.e., open boundary curve) and nonspherical bodies are also discussed,

2. METHODOLOGY

The proposed algorithm for limb/terminator extraction is summarized in Fig. 2. Image processing steps consist of 1) edge enhancement, 2) region segmentation, 3) boundary tracing, and

4) limb/terminator bifurcation. Steps 1 through 3 are based on well-established techniques: Figure 3 illustrates the result of applying the Sobel filter [11] (selected as a representative for edge enhancement techniques [11]-[15]) to the Miranda image shown in Fig. 1; Figure 4 shows the result of a histogram-based segmentation technique [5], [16]-[17] used in detecting the object region; and Figure 5 demonstrates the tracing of boundary points [18]- [19] which completes the preprocessing steps required prior to the limb/terminator bifurcation. However, step 4 is the essence of this paper, culminating in a robust limb and terminator extraction methodology for planetary images.

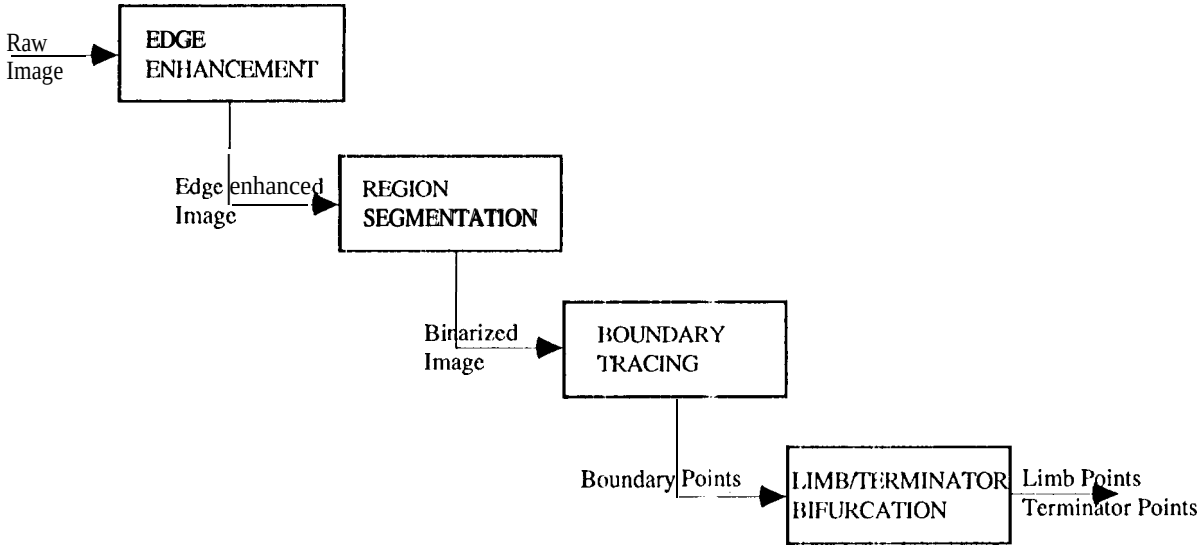

Fig. 2. The limb/terminator extraction algorithm.

Fig. 3. The edge-enhanced image of Miranda.

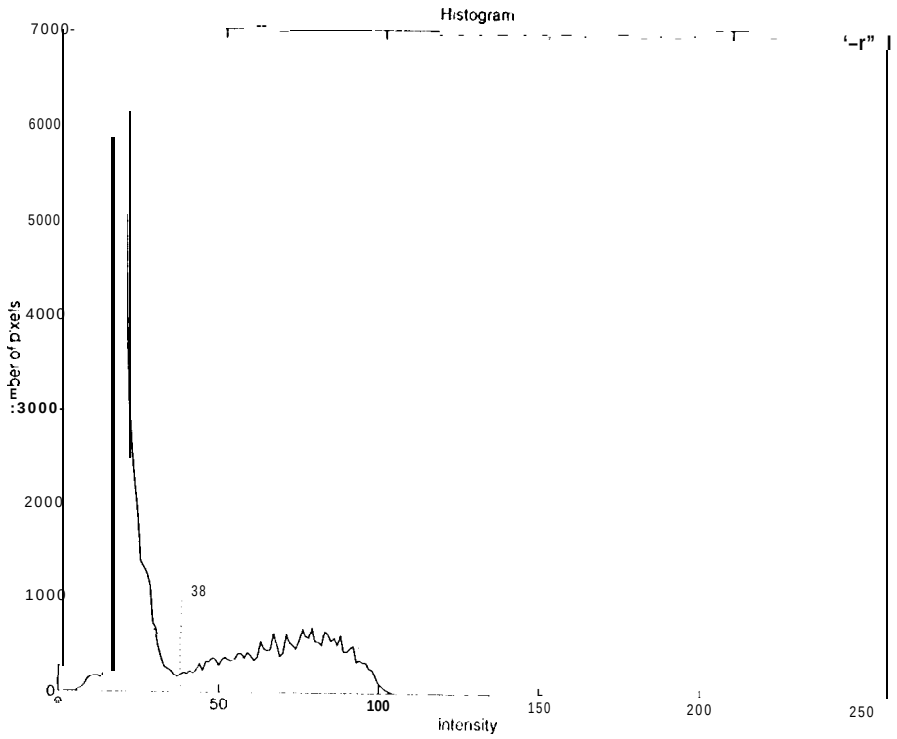

(a)

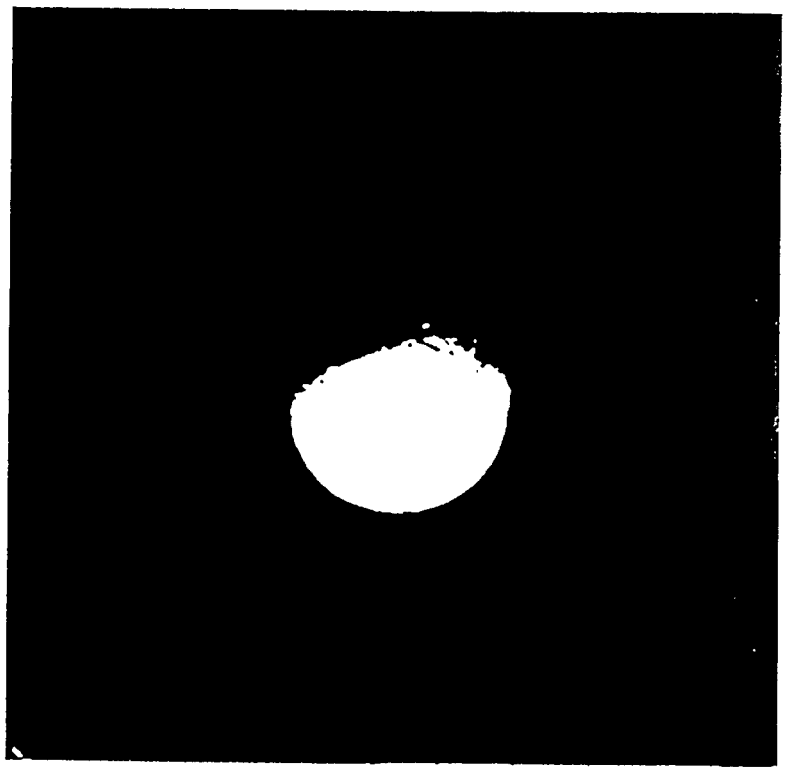

(h)

Fig. 4. The histogram of the image shown in Fig. 1 based on selected points with high local edge gradient magnitude and the binarized image resulting from applying the selected threshold (which is 38 for this image).

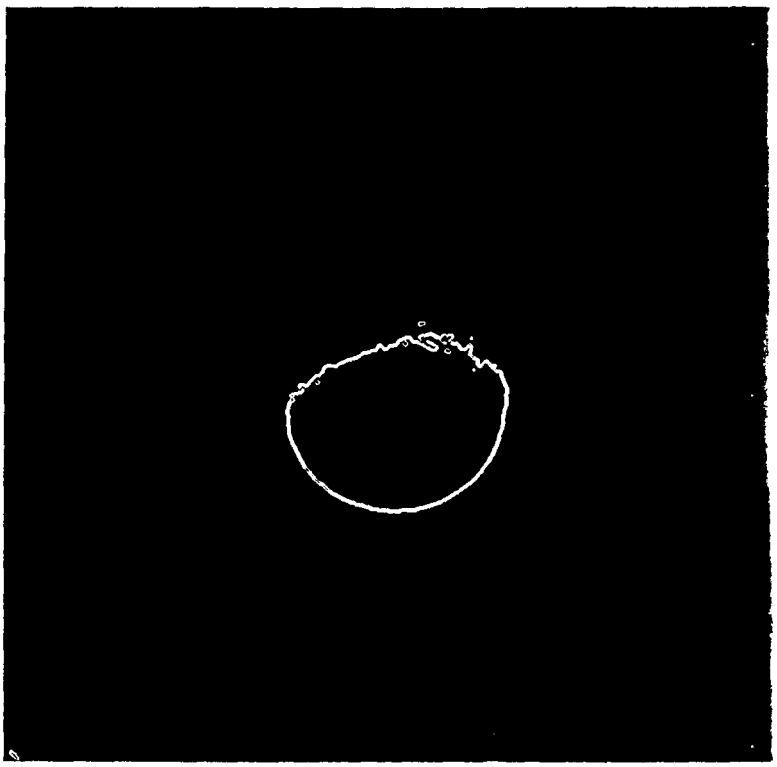

Fig. 5. Selected boundary points for the Miranda image.

As mentioned earlier, the task of differentiating limb segments from terminator segments can be quite difficult. Instinctive solutions such as high/low edge-strength segmentation [6] and locating the largest separation pair of boundary points (assuming spherical bodies) are found to be inadequate. In this paper, we propose a more robust solution by locating the harmonized segment of the parametrized boundary curve to differentiate the limb segment from terminator (assuming that the edge points are successfully clustered for each object).

Let's consider the case of spherical objects, the parametrized curve of the true boundary can be given by

$$x(t) = R\cos(2\pi t + \phi) + \mu_x;$$

$$y(t) = R\sin(2\pi t + \phi) + \mu_y; \qquad (1)$$

where t is the path length normalized to 1, R is the unknown radius, ϕ is the unknown phase shift caused by selecting an arbitrary starting point, and $[\mu_x, \mu_y]$ are the unknown center coordinates. Thus synchronization of $x(t)$ and $y(t)$ can be achieved by applying the derivative operator $\mathbf{D}_t$ and normalizing by 2π, i.e.,

$$\tilde{y}(t) = \frac{1}{2\pi}\mathbf{D}_t[y(t)\ 1 = R\cos(2\pi t + \phi) + \mu_x - \mu_x = x(t) - \mu_x. \qquad (2)$$

Note $\mathbf{D}_t$ operation can be performed by convolving with (he kernel described in Eq. (l).

Hence, $x(t)$ can be compared with $\tilde{y}(t)$ by searching in a one-dimensional μ_x-parameter space to locate the true μ_x, which can be accomplished with an accumulator of votes, giving one vote to each position that lines up (vis-a-vis the Hough transform).

To determine the matched section of $x(t)$ and $\tilde{y}(t)$, an accumulator A_k for a quantized range of μ_x is set up to register every point that satisfies

$$|(x_i - \mu_k) - \tilde{y}_i| < \tau, \qquad (3)$$

where xi is the indexed array of x(t), $\tilde{y}_i$ is the indexed array of $\tilde{y}(t)$, μ_k is the indexed array of candidate μ_x values, and τ represents the error tolerance. In our applications, τ is set to be 5% of the range of $\tilde{y}(t)$.

μ_x is then estimated as follows:

a) Find the maximum of $A_k(\hat{A})$;

b) Locate the indices corresponding to the range of μ_x at half-height, i.e.,

k_a and k_b such that $A_k > \hat{A}/2$ fork. $\leq k \leq k_b$;

c) Find the midpoint index k^* (i.e., $k^* = (k_a + k_b)/2$) and

calculate the new tolerance $\tau^* = (k_b - k_a + 1)\,\tau/2$ for recovering the matched segment,

d) Extract the longest chain of points which satisfy $I(x_i - \mu_{k*}) - \tilde{y}_i I < \tau^*$.

This "half-width half-height" peak detection method [20] can allievate the dependence on the tolerance setting. For example, a small tolerance value tends to produce a wide peak, so the final matching tolerance τ^* will expand accordingly,

Figure 6 shows the result of this process. Notice the relatively well-behaved characteristic of $\tilde{y}(t)$ in the matched segment (also shown as a thick line on x(t)) compared to the noisy terminator segment, Although the differential operator $\mathbf{D}_t$ makes $y(t)$ noisier, the noise in the terminator segment is accentuated to a much greater magnitude, which somewhat simplifies the matching process by giving rise to a distinct peak in the μ_x -accumulator space.

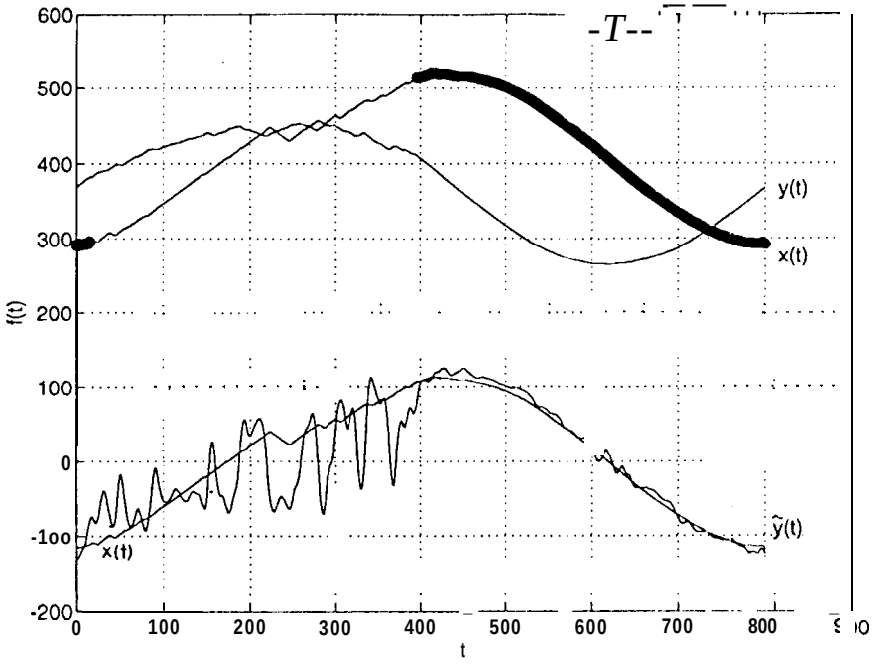

(a)

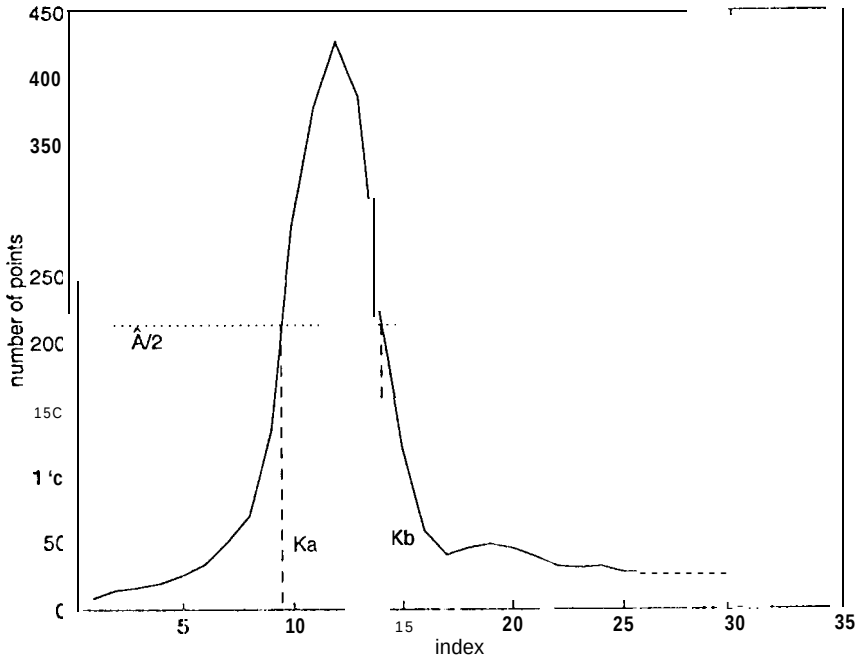

(b)

Fig. 6. Boundary curve comparisons pre- and post-harmonization and the accumulator peak detection.

The consistency in the t parameter for $x(t)$, $y(t)$, and $\tilde{y}(t)$ is also a plus, Although the t-spacing between points is not constant since we estimate Δt to be 1 for horizontal and vertical steps and $\sqrt{2}$ for diagonal steps, the comparison and synchronization between $x(t)$ and $\tilde{y}(t)$ are achieved in unison since one measured parametric function is used to reference another, and both functions possess the same t-spacing. To some extent, this shows a robustness toward geometric distortions compared to other techniques that rely on matching to synthetic functional templates with prespecified parameters.

Given the indices of boundary points from the parametric equations, the limb and terminator segments on the image plane can be separated, and Figure 7 depicts the results of the proposed limb/terminator bifurcation with the limb points highlighted by the thick. curve.

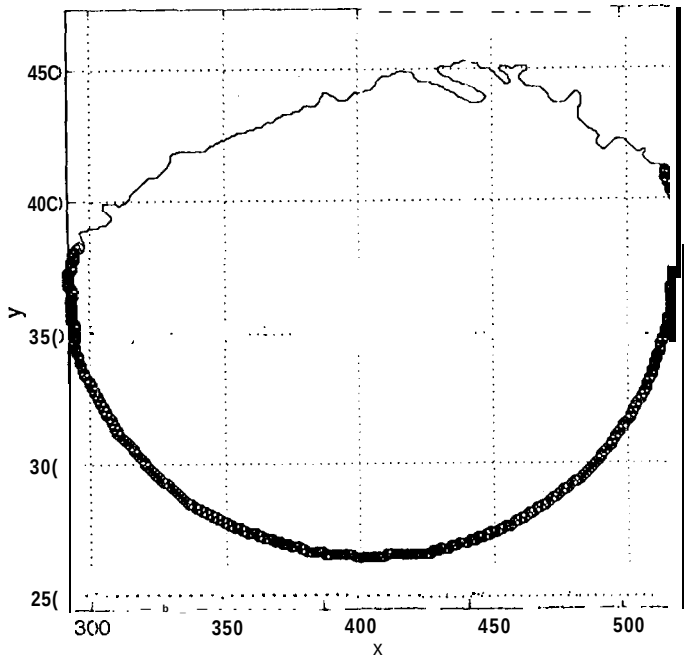

Fig. 7. The limb/terminator extraction of the Miranda image.

The situation of having a partially-viewed object (i.e., open boundary curve) is of no concern here, because in most cases the limb and terminator extraction will only be applied during the distant encounter of a planetary body to initially acquire, characterize, map, and estimate its motion to aid in planning future spacecraft maneuvers and pointing. However, the same methodology can still be applied, if needed:

$$x(t) = R\ cos(2\pi ft + \phi) + \mu_x ;$$

$$y(t) = R\ sin(2\pi ft + \phi) + \mu_y ; \qquad (4)$$

where f is the frequency and will be less than 1 because of less than one complete sinusoidal cycle due to the open curve. This means $x(t)$ can be compared with $\mathbf{D}_t\ [y(t)]/2\pi$ by searching in a two-dimensional $[\mu_x, f]$-parameter space. As long as a significant portion of the limb is present, this methodology is still applicable.

Although we formulate a solution to handle spherical (or near-spherical) bodies, this methodology can be extended to nonspherical objects. For example, if the true boundary is an ellipse,

$$x(t) = RX\ cos(2\pi t + \phi) + \mu_x ;$$

$$y(t) = R_y sin(2\pi t + \phi) + \mu_y ; \qquad (5)$$

and

$$\tilde{y}(t) = \frac{1}{2\pi}\mathbf{D}_t\,[y(t)] = \frac{R_y}{R_x}[\,R_x\ cos(2\pi t + \phi) + \mu_x - \mu_x\,] = \frac{R_y}{R_x}[\,x(t) - \mu_x\,]. \qquad (6)$$

This means x(t) can be compared with $\tilde{y}(t)$ in a two-dimensional $[\mu_x, R_y/R_x]$-space to determine the two unknown parameters.

For irregularly shaped bodies, piecewise shape decomposition can be accomplished by matching to different geometries (e.g., line, circle, ellipse, etc.), and the harmonization of $x(t)$ and $y(t)$ may

require some other form of operators besides $\mathbf{D}_t$. Some sort of smoothing or ellipsoidal approximation may also be applicable. Future research will address this issue further, which is essential for the exploration of small bodies (i.e., comets and asteroids).

3. EXPERIMENTS

Experiments with Voyager image data have given us the data for assessing the performance and robustness of the proposed algorithm for various planetary images. Voyager image data are available in CD-ROMs through the Planetary Data System at the Jet Propulsion Laboratory. The images are 800 by 800 with 8-bit resolution. Test algorithms are coded in C on the Sun Sparc10 workstation.

3.1. *Results*

Figures 8-10 demonstrate the robustness of the proposed limb/terminator extraction for different types of planetary terrains and terminator characteristics. These three illustrations are selected because of they are relatively difficult compared to other images. Figure 8 depicts the half-moon shape which is the worst-case situation for our ideal circle assumption, Eq. (1), because the perimeter is at the minimum deviation from 2π. This issue is discussed further in the next section. Figure 9 depicts the crescent shape with the terminator side which is equally smoothed compared to the limb side. Finally, Figure 10 shows a dark region on the limb side which is excluded after the segmentation process. Even with less than half the circle, the correct limb points are successfully extracted. The sharp peak of the accumulator A_k (shown in Figs. 8c, 9c, and 10c) ensures the robustness of μ_x and τ^* calculation based on the. simple "half-width half-height" peak detection method.

Other planetary images tested include images from Uranus, Ariel, Oberon, Titania, Umbriel, Dione, Enceladus, Epimethe, Iapetus, Callisto, Mimas, Rhea, Tethys, Titan, Europa, Ganymede, and Jupiter. A total of 50 images were tested, and the algorithm properly and satisfactory (based

on visual inspection) separated the limb and terminator in every case without adjusting any of the required parameter settings.

Timing estimated for the whole process is about 10 seconds on **the Sun** Spare 10 workstation. Currently available flight processors (25-40 MIPS) will probably run 2-3 times slower. Because of the vast distance encountered in space exploration, this timing number is well within the established frame rate for spacecraft pointing operations, even with a much slower processor (a fastest frame rate is probably between 10-60 minutes/frame for this t ype of processing during the initial acquisition phase).

(a)

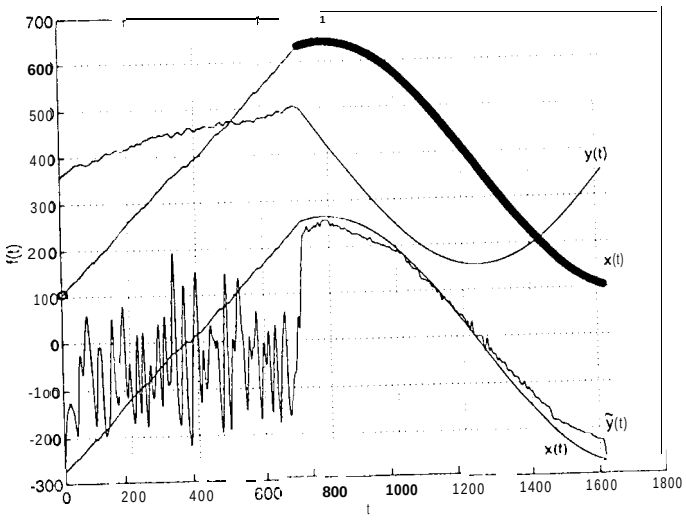

(b)

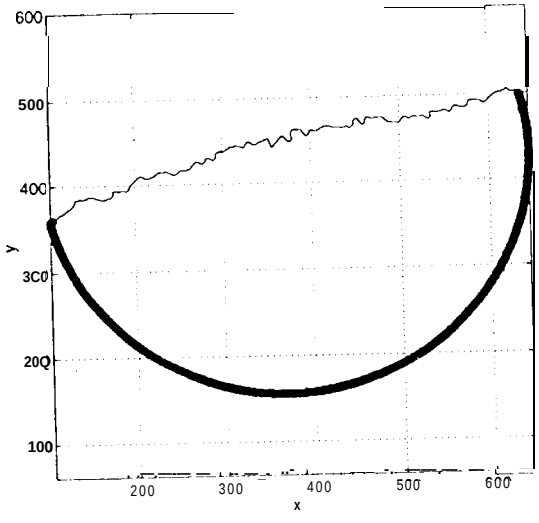

(d)

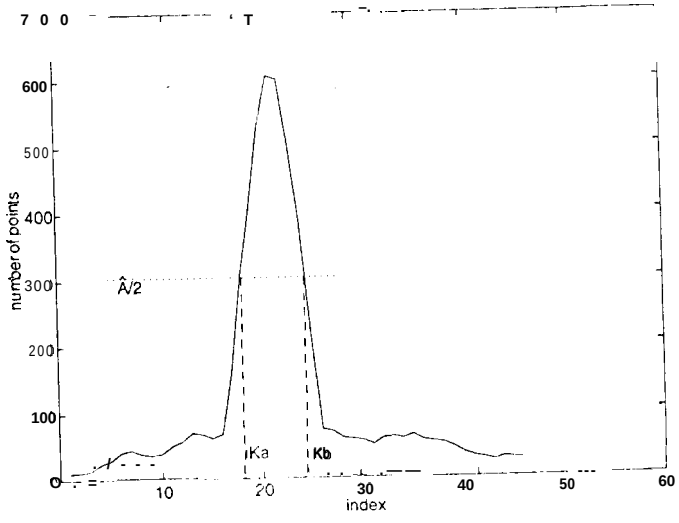

(c)

Fig. 8. Voyager image of Callisto (a Jupiter moon) and the corresponding limb/terminator extraction.

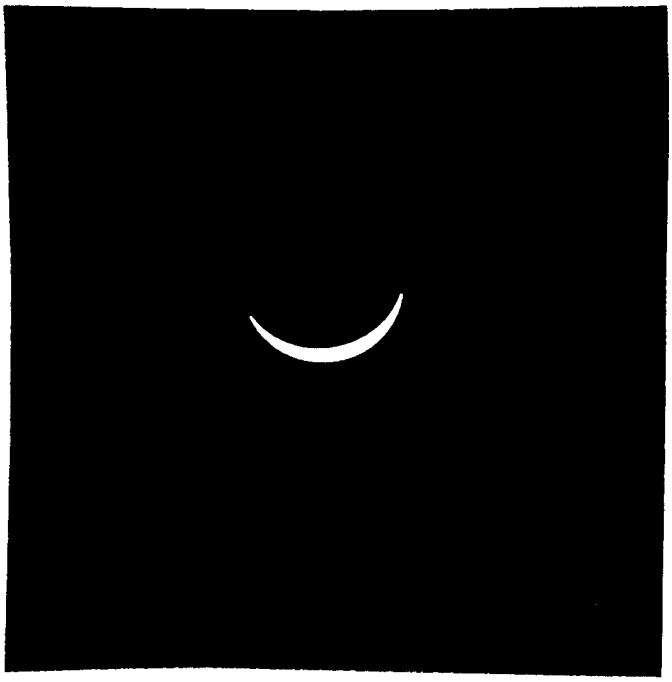

(a)

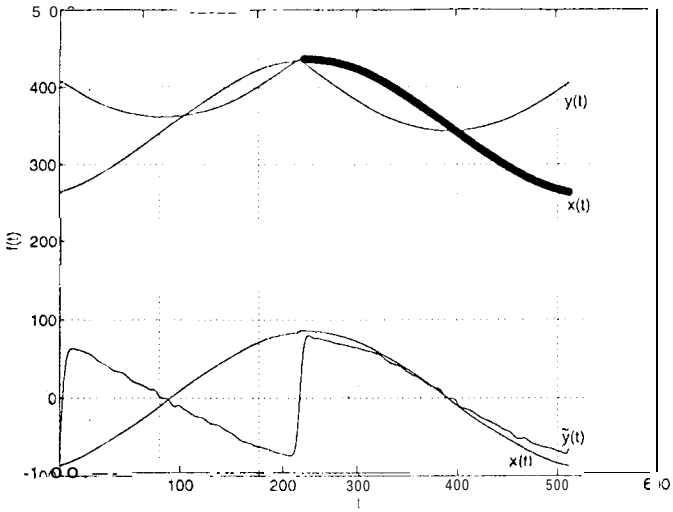

(b)

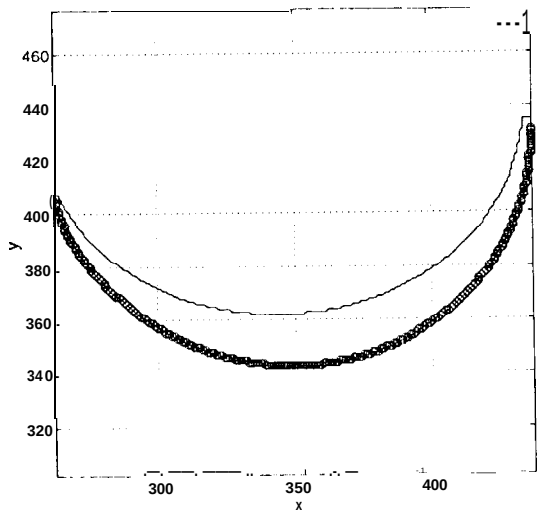

(d)

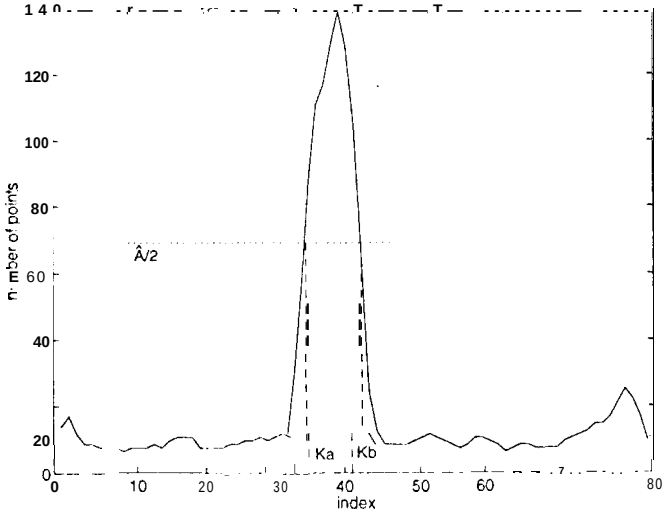

(c)

Fig. 9. Voyager image of Uranus and the corresponding limb/terminator extraction.

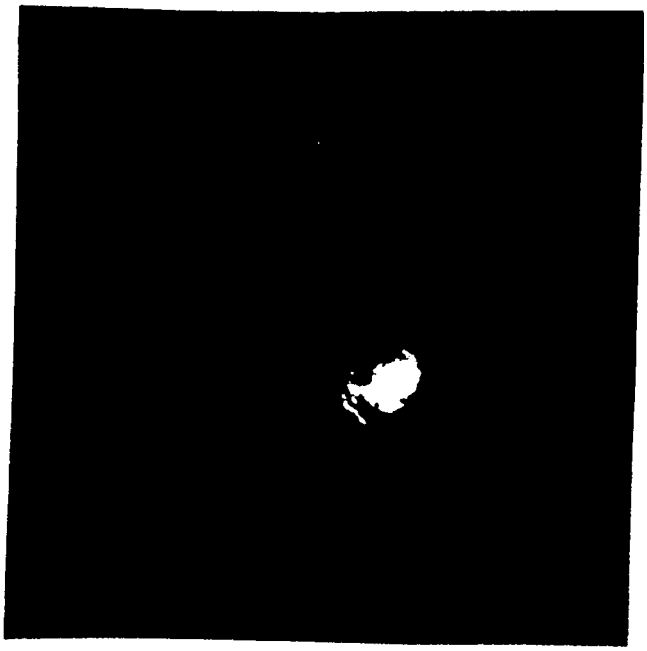

(a)

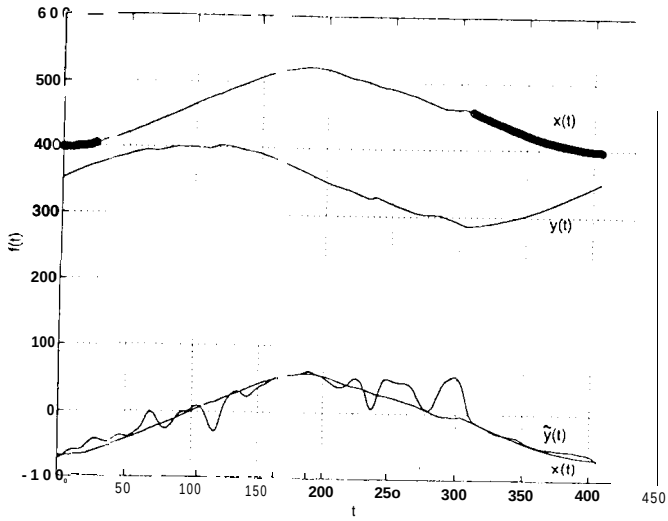

(b)

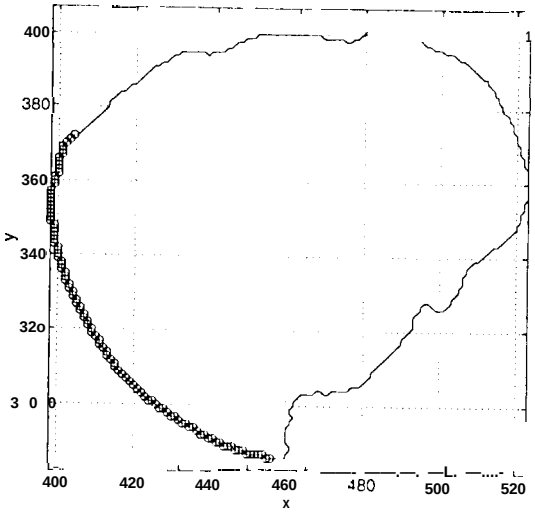

(d)

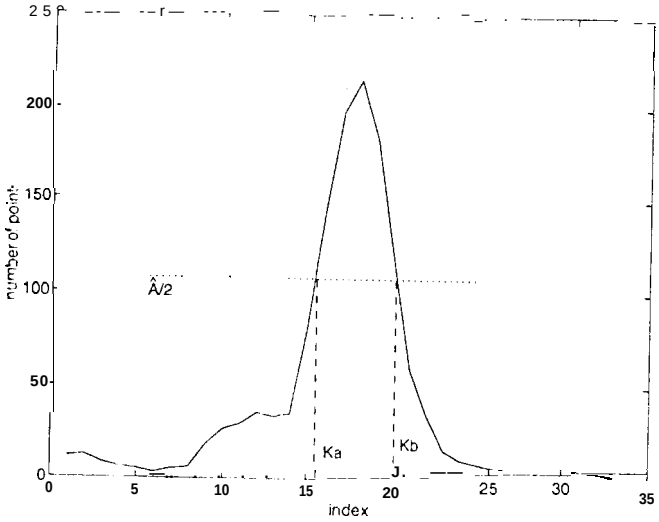

(c)

Fig. 10. Voyager image of Iapetus (a Saturn moon) and the corresponding limb/terminator extraction.

3.2. *Discussion*

In almost every case, the amplitude of $\tilde{y}(t)$ *is* attenuated by a small amount, which does not change the matching (limb/terminator bifurcation) results. This is due to the fact that the measured parametric equations are not completely sinusoidal with exactly 1 Hz frequency, Let's consider the worst case situation with the half-moon shape:

$$x(t) = \begin{cases} R\ cos(2\pi ft + \phi) + \mu_x & \text{for } 0 \le t \le \pi/(\pi+2). \\ t - \pi/(\pi+2) & \text{for } \pi/(\pi+2) \le t \le 1 \end{cases},$$

$$y(t) = \begin{cases} R\ sin(2\pi ft + \phi) + \mu_y & \text{for } 0 \le t \le \pi/(\pi+2). \\ \mu_y & \text{for } \pi/(\pi+2) \le t \le 1 \end{cases}, \qquad (7)$$

and

$$\tilde{y}(t) = \frac{1}{2\pi} \mathbf{D}_t [y(t)] = \begin{cases} Rf\ cos(2\pi ft + \phi) + \mu_x & \text{for } 0 \le t < \pi/(\pi+2). \\ 0 & \text{for } \pi/(\pi+2) < t \le 1 \end{cases}, \qquad (8)$$

where $f = (\pi+2)/2\pi \approx 0.82$, As shown in Eq. (8), the amplitude of $\tilde{y}(t)$ *is* attenuated by this factor for the ideal half-moon case. For any other shape, the attenuation will be less because of the longer terminator path length.

If a more precise matching is required, we can search in a two-dimensional $[\mu_x, f]$-parameter space, which is the same as the open boundary curve formulation, Eq. (4). However, in most cases, the traced boundary through the noisy terrains along the terminator will cause the perimeter to be much closer to 2π (i.e., $f \rightarrow 1$), and as a result the ideal formulation, Eq. (1), is adequate for our applications.

Another formulation that may alleviate this shortened path-length problem is to find the limb segment which satisfies

$$\mathbf{D}_t^2[x(t)] + \mathbf{D}_t^2[y(t)] = 1, \qquad (9)$$

where t is the unnormalized path-length. However, we found that the noise problem becomes more severe here, and the required matching for Eq. (9) is not as robust as the proposed technique, which requires only one different ial operator.

4. SUMMARY AND CONCLUSIONS

Future space exploration will require onboard autonomous target recognition systems to point instruments and maneuver spacecraft with great efficiency, a means for implementing capable, low-cost planetary exploration. We address a particular problem of extracting planetary limb and terminator which is a precursor to characterizing planet shape and size, estimating target-relative positions, and planning of science data acquisition and spacecraft maneuver sequences. In searching for a robust solution for a variety of planetary images, we developed a novel and efficient technique to bifurcate the extracted planet boundary which allows reliable determination of the limb and terminator points based on real planetary images. Relying on the spherical nature of planetary bodies, harmonization of the parametric equation of the boundary curve is achieved with a simple differential operator. Matching the corresponding circular arc is simply done with a Hough transform-like accumulator, Experiments with many different types of planetary images using Voyager data led us to believe that the proposed methodology is robust for celestial scenes.

The attractiveness of the proposed limb/terminator bifurcation approach is that it can be extended to accommodate irregularly shaped bodies (i.e., asteroids, comets, and other small bodies). Although we have discussed briefly the formulations for partially-viewed and ellipsoidal objects, more research will be required to derive other type of operators that can harmonize non-circular or non-ellipsoidal parametric functions and allow piecewise shape-decomposition that can address any arbitrary shape, and the problem of multiple bodies and occlusions will also be addressed.

ACKNOWLEDGMENTS

The research described in this paper was carried out by the Jet Propulsion Laboratory, California Institute of Technology, under a contract with the National Aeronautics and Space Administration.

REFERENCES

1. S. Udomkesmalee, G. E. Sevaston, and R. H. Stanton, Toward an autonomous feature-based pointing system for planetary missions, *Proc. Space Guidance, Control, and Tracking,* SPIE 1949, 1993, 2-14.

2. K. S. Fu and J. K. Mui, A survey on image segmentation, *Patter-n Recognition* 13, 1981, 3-16.

3. R. M, Haralick and L. G. Shapiro, image segmentation techniques, *Comput. Graphics Image Process. 29, 1985, 100-132.*

4. S. P. Synnott, A. J. Donegan, J. E. Riedel, and J. A. Stuve, Interplanetary optical navigation, in *Proceedings, Astrodynamics Conference, Williamsburg, 1986,* pp. 192-206.

5. J. S. Weszka, R. N. Nagel, and A. Rosenfeld, A threshold selection technique, *IEEE Trans. Comput. C-23, 1974, 1322-1326.*

6. C.-C. Chu, D. Q. Zhu, S. Udomkesmalee, and M. 1. Pomerantz, Realization of autonomous image-based spacecraft pointing systems: planetary flyby example, *Proc. Acquisition, Trucking, and Pointing VIII, SPIE 2221, 1994, 27-40.*

7. R. L. Staehle, D. S. Abraham, J. B. Carraway, C. G. Salvo, R. J. Terrile, R. A. Wallace, and S. S. Weinstein, Exploration of Pluto, *Acta Astronautic 30,* 1993, 289-310.

8. R. O. Duda and P. E. Hart, Use of the Hough transform to detect lines and curves in pictures, *Communication ACM 15, 1972,* 11-15.

9. F. Mokhtarian and A. Mackworth, Scale-based description and recognition of planar curves and t we-dimensional shapes, *IEEE Trans. Pattern Anal. Mach. Intell. 8,* 1986, *34-43.*

10. S. Udomkesmalee, Feature recognition of two-dimensional object scenes using contour curvature representation, in *Automatic Control in Aerospace 1992* (D. B. DeBra and E. Gottzein, Eds.), pp. *451-456,* Permagon Press, Oxford, 1993.

11. I. Sobel, Camera models and machine perception, *Stanford Al Memo 121*, Department of Computer Science, Stanford University, 1970.

12. R. Kirsch, Computer determination of the constituent structure of biological images, *Comput. Biomed. Res. 4*, 1971, 315-328.

13. D. Marr and E. Hildreth, Theory of edge detection, *Proc. R. Sot. Lend. B 207, 1980, 187-217.*

14. R. M. Haralick, Digital step edges from zero crossing of second directional derivatives, *IEEE Trans. Pattern Anal. Mach. Intell. 6, 1984, 58-68.*

15. J. F. Canny, A computational approach to edge detection, *IEEE Trans. Pattern Anal. Mach. Intell. 8, 1986, 679-698.*

16. M. I. Sezan, A peak detection algorithm and its application to histogram-based image data reduction, *Comput. Graphics Image Process. 49, 1990,36-51.*

17. A. P. Witkin, Scale-space filtering, in *Proceedings, 8th Int. Joint Conf. Artificial intelligence, Karlsruhe, West Germany, 1983,* pp. 1019-1022.

18. E.R. Davies, *Machine Vision: Theory, Algorithms, Practicalities,* Academic Press, San Diego, California, 1990.

19. F. P. Preparata and M. I. Shames, *Computational Geometry*, Springer-Verlag, New York, 1985.

20. M. S. Scholl and S. Udomkesmalee, Algorithms for detection of correlation spots, *NASA Tech Briefs 17, 1993, 132-133.*